

# GRIL-Calib: Targetless Ground Robot IMU-LiDAR Extrinsic Calibration Method using Ground Plane Motion Constraints

TaeYoung Kim<sup>1</sup>, Gyuhyeon Pak<sup>2</sup> and Euntai Kim<sup>2,\*</sup>

**Abstract**— Targetless IMU-LiDAR extrinsic calibration methods are gaining significant attention as the importance of the IMU-LiDAR fusion system increases. Notably, existing calibration methods derive calibration parameters under the assumption that the methods require full motion in all axes. When IMU and LiDAR are mounted on a ground robot the motion of which is restricted to planar motion, existing calibration methods are likely to exhibit degraded performance. To address this issue, we present *GRIL-Calib*: a novel targetless Ground Robot IMU-LiDAR Calibration method. Our proposed method leverages ground information to compensate for the lack of unrestricted full motion. First, we propose LiDAR Odometry (LO) using ground plane residuals to enhance calibration accuracy. Second, we propose the Ground Plane Motion (GPM) constraint and incorporate it into the optimization for calibration, enabling the determination of full 6-DoF extrinsic parameters, including theoretically unobservable direction. Finally, unlike baseline methods, we formulate the calibration not as sequential two optimizations but as a single optimization (SO) problem, solving all calibration parameters simultaneously and improving accuracy. We validate our *GRIL-Calib* by applying it to three public real-world datasets and comparing its performance with that of existing state-of-the-art methods in terms of accuracy and robustness. Our code is available at <https://github.com/Taeyoung96/GRIL-Calib>.

**Index Terms**— Calibration and identification, Sensor Fusion, Optimization, Mobile Robot.

## I. INTRODUCTION

LiDAR (Light Detection And Ranging) acquires more accurate 3D information than other sensors, making it broadly applicable to a variety of robotic applications such as ego-motion estimation [1], localization [2] and mapping [3] system. However, LiDAR has the drawback that when it is applied to fast motion, it is vulnerable to motion distortion. Recently, to overcome the drawback, LiDAR has been used in conjunction with IMU (Inertial Measurement Unit) [4], [5], [6]. The IMU effectively compensates for the motion distortion of the LiDAR, as it measures acceleration and angular velocity at a high frequency. Obviously, accurate extrinsic calibration is a fundamental requirement in the IMU-LiDAR fusion system. Extrinsic calibration refers to the process of establishing the spatial transformations between IMU and LiDAR, thereby aligning the measurements from the two sensors. If the extrinsic calibration is not accurate enough, the

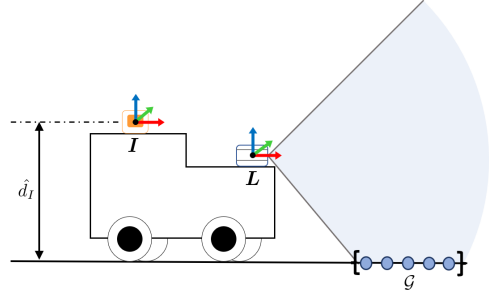


Fig. 1: Illustration of a ground robot equipped IMU ( $I$ ) sensor and LiDAR ( $L$ ) sensor. We leverage the IMU height from the ground ( $\hat{d}_I$ ) as minimal prior knowledge and the LiDAR ground segmentation points ( $\mathcal{G}$ ) for IMU-LiDAR extrinsic calibration.

fusion of IMU and LiDAR becomes less effective, leading to significant degradation in overall performance [7].

Therefore, a lot of research has been conducted regarding the extrinsic calibration between IMU and LiDAR, and the research can be divided into two directions: target-based and targetless approaches. Target-based approach uses known, predefined objects such as cylinders [8] to estimate the spatial transformations between IMU and LiDAR. Target-based approach is relatively accurate, but it has the shortcoming that predetermined targets are required. On the other hand, the targetless approach does not use any predefined objects for calibration, receiving much attention due to ease of use and repeatability. Instead, the targetless method requires comprehensive excitation motion of both sensors to activate all Degrees of Freedom (DoF). Achieving this motion is straightforward for handheld devices with integrated IMU and LiDAR sensors, as they can easily perform a full range of motions. However, for ground robots, it becomes a significant challenge because their motion is limited to planar motion. Furthermore, from a theoretical perspective, the lack of full motion will make the rank of Fisher information matrix (FIM) less than its dimension, and the degenerate or rank-deficient FIM will cause the estimated calibration parameters to have high uncertainty or not to become unique. To address the issue, some papers perform observability analysis [9], [10], [11], but the analysis only identifies unobservable directions and does not directly estimate calibration parameters.

In this paper, we present *GRIL-Calib*: novel targetless Ground Robot IMU-LiDAR extrinsic Calibration method. To address the aforementioned degenerate problem, we utilize a ground plane motion (GPM) constraint. The GPM provides

\* is that the corresponding author.

<sup>1</sup>TaeYoung Kim is the Department of Vehicle Convergence Engineering, Yonsei University, Seoul 03722, South Korea [tyoung96@yonsei.ac.kr](mailto:tyoung96@yonsei.ac.kr)

<sup>2</sup>Gyuhyeon Pak and Euntai Kim are with the Department of Electrical and Electronic Engineering, Yonsei University, Seoul 03722, South Korea  [{ghpak, etkim}@yonsei.ac.kr](mailto:{ghpak, etkim}@yonsei.ac.kr)

geometric information about the robot’s motion and allows the full 6-DoF extrinsic parameters even when some of the extrinsic parameters are unobservable. The extrinsic calibration problem between IMU and LiDAR for ground robots is depicted in Fig 1. Similar constraints related to the ground have been proposed for LiDAR odometry (LO) [12] or visual-inertial odometry (VIO) [13]. However, we propose a ground plane motion (GPM) constraint specifically focused on the extrinsic calibration of the IMU and LiDAR. The proposed method leverages a motion-based approach and integrates ground observation, thereby offering a user-friendly and accurate solution for extrinsic calibration of the IMU and LiDAR mounted on the ground robot. The key contributions of this paper are summarized as follows:

- We propose a novel extrinsic calibration method of IMU-LiDAR fusion system on a ground robot and thus does not need to satisfy full excitation motion.
- To improve the performance of the calibration, we proposed a novel LiDAR Odometry (LO) that exploits ground plane observations. The ground plane residuals are incorporated into an Iterative Error State Kalman Filter (IESKF) to reduce drift around the z-axis.
- We propose Ground Plane Motion (GPM) constraints and apply the constraint to the nonlinear optimization for calibration. The GPM enables us to address parameters including unobservable direction and also improve calibration accuracy.
- In the nonlinear optimization for calibration, we formulate the calibration of the translation and rotation parameters as a Single Optimization (SO) problem solve parameters simultaneously. The baseline methods, however, calibrate the two parameters separately and sequentially, degrading the calibration accuracy.
- We validate our *GRIL-Calib* on M2DGR [14], Hilti [15], and S3E [16] datasets where it achieves excellent results compared to state-of-the-art targetless methods. We have open-sourced<sup>1</sup> our algorithm to benefit the broader robotics community.

The rest part of this paper is organized as follows: Section II presents a comprehensive review of recent IMU-LiDAR calibration methods. In Section III, we present the system overview of *GRIL-Calib* and describe each key part in detail at Section IV and Section V. Section VI describes the experiments performed on various real-world datasets and the analysis of the results. Finally, Section VII provides conclusions and discusses future work.

## II. RELATED WORK

In early IMU-LiDAR calibration research, an arbitrary target is required for calibration [8], [17]. However, the target-based method is not practical, so targetless calibration methods have been studied more recently. Subodh *et al.* [18] formulate a motion-based calibration based on the Extended Kalman Filter (EKF). Additionally, Lv *et al.* [19] utilizes a continuous-time trajectory formulation based on B-Spline.

Also, OA-LICalib [11] which extends their previous works [19], proposes two observability-aware modules designed to address the degenerate case. Unfortunately, the proposed observability-aware module is designed to only reject unnecessary motion. FAST-LIO2 [4] is an accurate LiDAR-inertial odometry (LIO) algorithm based on an Iterated error state Kalman filter (IESKF) which include extrinsic calibration parameters. Due to the strong nonlinearity, the performance of the LIO system is highly dependent on accurate initial states. To get an accurate estimate of the initial states, Zhu *et al.* [20] propose the optimization-based algorithm that aligns angular velocity and acceleration. Existing approaches [18], [11], [20] require sufficient motion in all axes of the sensor to obtain accurate results. These methods are practical when applied to handheld devices that can move freely in various directions. However, existing methods encounter challenges when applied to ground robots where motion is limited to planar motion. In contrast, our method utilizes ground observation that can easily be observed by a ground robot to obtain accurate 6-DoF extrinsic parameters, even in the absence of sufficient motion in all axes. Recently, an extended Kalman filter (EKF) based IMU-LiDAR calibration algorithm utilizing a GNSS observation model in planar motion has been proposed [7]. However, it requires an additional GNSS sensor, while our proposed algorithm calibrates IMU-LiDAR without additional sensors.

## III. SYSTEM OVERVIEW

The overall system of *GRIL-Calib* comprises two primary stages: pre-processing and optimization, as shown in Fig. 2. Our framework is motivated by [20]. The first stage is pre-processing, which generates additional information that is critical for the following optimization stage. Specifically, the pre-processing stage performs the following key tasks:

- *Ground Observation via ground segmentation*, where ground points are extracted from LiDAR data, facilitating the estimation of the LiDAR sensor’s relative orientation to the ground.
- *Lidar Odometry (LO)*, which enhances LO performance by utilizing the extracted ground plane and incorporating a proposed ground plane residual.
- *IMU Processing*, involving the pre-processing of IMU measurements and the calculation of the IMU’s relative orientation to the ground using the Madgwick filter [21].
- *Data Synchronization*, aimed at determining the approximate time offset between IMU and LiDAR data using cross-correlation methods. Notably, this process aligns with the approach proposed in [20].

The second stage is optimization, which aims to optimize the extrinsic calibration parameters by utilizing the data acquired in the preprocessing stage. In this optimization stage, we apply three types of constraints: unified temporal-spatial constraints based on angular velocity and linear acceleration, as well as proposed Ground Plane Motion (GPM) constraints. The GPM constraint ensures that the robot’s motion remains on the ground and is integrated into the objective function to achieve precise extrinsic calibration

<sup>1</sup><https://github.com/Taeyoung96/GRIL-Calib>

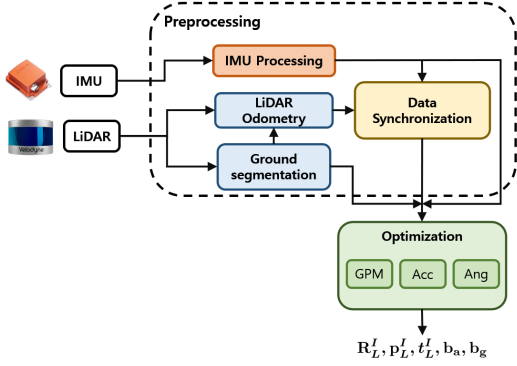


Fig. 2: The overview of proposed *GRIL-Calib* system. During the optimization stage (Green Box), we use 3 constraints. See Section V for more details.

while limiting planar motion. In contrast [20], where each type of objective function is optimized individually and sequentially, we simultaneously optimize all three types of constraints by assigning different values of weights to each objective. This approach improves performance compared to the method in [20].

Throughout the paper, we use the following notations: LiDAR frame denotes  $\{L\}$ , IMU frame denotes  $\{I\}$ ,  $\mathbf{R}_L^I \in SO(3)$  is the rotation matrix from IMU frame to LiDAR frame.  $\mathbf{p}_L^I \in \mathbb{R}^3$  is the translation vector from the IMU frame to the LiDAR frame.  $t_L^I \in \mathbb{R}$  is the time offset between IMU and LiDAR.  $\mathbf{b}_a, \mathbf{b}_g \in \mathbb{R}^3$  means the acceleration bias and angular velocity bias of the IMU, respectively.

#### IV. PREPROCESSING

In the preprocessing stage, we obtain some parameters and the sensor measurements which will be used in the subsequent the optimization stage.

##### A. Ground Observation via LiDAR Ground Segmentation

First, the ground is segmented from the LiDAR input. LiDAR ground segmentation aims to obtain the rotation matrix  $\mathbf{R}_L^G$  of the LiDAR with respect to the ground. When the current LiDAR scan  $\mathcal{P}$  is presented, we extract a set of ground points  $\mathcal{G}$  using Patchwork++ [22], a state-of-the-art (SOTA) ground segmentation algorithm. Then, we apply the Principal Component Analysis (PCA) to the covariance matrix  $\mathcal{C}_G$  of the ground points  $\mathcal{G}$  identifying a normal vector  $\mathbf{n}_L = (a_L, b_L, c_L)^T$  of the ground plane

$$a_L x + b_L y + c_L z + d_L = 0 \quad (1)$$

where  $\mathbf{n}_L$  implies a normal vector to the ground in the LiDAR coordinate  $\{L\}$ . We also define a normal vector  $\mathbf{n}_G = (0, 0, 1)^T$  with respect to the ground coordinate  $\{G\}$ . From the two normal vectors  $\mathbf{n}_L$  and  $\mathbf{n}_G$ , we obtain a rotation matrix  $\mathbf{R}_L^G$  from  $\{G\}$  frame to  $\{L\}$  frame by

$$\mathbf{R}_L^G = \exp([\phi_{GL} \mathbf{n}_{GL}]_{\times}) \quad (2)$$

where  $\phi_{GL} = \arccos(\mathbf{n}_G^T \mathbf{n}_L) \in \mathbb{R}$  and  $\mathbf{n}_{GL} = \mathbf{n}_G \times \mathbf{n}_L \in \mathbb{R}^3$  denote the rotation angle and vector between  $\{G\}$  and  $\{L\}$ ,

respectively.  $[\cdot]_{\times}$  denotes the skew-symmetric matrix, and  $\exp(\cdot)$  denotes the exponential map.

##### B. LiDAR Odometry Utilizing the Ground Plane Residual

We use Iterated Error state Kalman Filter (IESKF) to obtain LiDAR Odometry (LO) with a similar procedure to [20]. However, we improved the performance of LO by exploiting the assumption that *ground robot is constrained to movement on a 2D plane*. When we define the state vector  $\mathbf{x}_k$  of the LiDAR by

$$\mathbf{x}_k = [\log(\mathbf{R}_{L_k}), \mathbf{p}_{L_k}, \boldsymbol{\omega}_{L_k}, \mathbf{v}_{L_k}]^T \quad (3)$$

and its motion as follows,

$$\mathbf{x}_{k+1} = \mathbf{x}_k \boxplus (\Delta t \cdot \mathbf{F}(\mathbf{x}_k, \mathbf{w}_k)) \quad (4)$$

where  $\mathbf{F}(\mathbf{x}_k, \mathbf{w}_k) = [\boldsymbol{\omega}_{L_k}, \mathbf{v}_{L_k}, \boldsymbol{\varepsilon}_\omega, \boldsymbol{\varepsilon}_v]^T$ .  $\mathbf{R}_{L_k}$  represents the attitude from the initial LiDAR frame  $\{L_0\}$  to the LiDAR frame  $\{L_k\}$  at current time  $k$ , that is  $\mathbf{R}_{L_k} = \mathbf{R}_{L_k}^{L_0}$ ,  $\log(\cdot)$  denotes the logarithmic map.  $\mathbf{p}_{L_k} = \mathbf{p}_{L_k}^{L_0}$  represents the position of the LiDAR at current time  $k$ .  $\boldsymbol{\omega}_{L_k}$  and  $\mathbf{v}_{L_k}$  represent the angular and linear velocities of the LiDAR at time  $k$ , respectively.  $\mathbf{w}_k = [\boldsymbol{\varepsilon}_\omega, \boldsymbol{\varepsilon}_v] \sim \mathcal{N}(\mathbf{0}, \mathbf{Q}_k)$  are a random walk noise represented by zero-mean Gaussian.  $\Delta t$  is the time interval between two consecutive scans, and the notation  $\boxplus$  represents the encapsulated “boxplus” operations on the state manifold [23].

The prediction step of the IESKF consists of the prediction of the state and the propagation of the covariance as follows,

$$\begin{aligned} \hat{\mathbf{x}}_{k+1} &= \bar{\mathbf{x}}_k \boxplus (\Delta t \cdot \mathbf{F}(\bar{\mathbf{x}}_k, \mathbf{0})) \\ \hat{\mathbf{P}}_{k+1} &= \mathbf{F}_{\bar{\mathbf{x}}} \bar{\mathbf{P}}_k \mathbf{F}_{\bar{\mathbf{x}}}^T + \mathbf{F}_{\mathbf{w}} \mathbf{Q}_k \mathbf{F}_{\mathbf{w}}^T \end{aligned} \quad (5)$$

where  $\hat{(\cdot)}$ ,  $\bar{(\cdot)}$ , and  $\tilde{(\cdot)}$  denote the predicted, error and optimal states, respectively;  $\bar{\mathbf{P}}_k$  and  $\mathbf{Q}_k$  are the covariance matrices for error state  $\tilde{\mathbf{x}}_k$  and noise  $\mathbf{w}_k$ , respectively.  $\mathbf{F}_{\bar{\mathbf{x}}}$  and  $\mathbf{F}_{\mathbf{w}}$  are the derivative of  $(\mathbf{x}_{k+1} \boxplus \hat{\mathbf{x}}_{k+1})$  with respect to  $\tilde{\mathbf{x}}$  and  $\mathbf{w}$  evaluated at zero, respectively. The notation  $\boxminus$  represents the encapsulated “boxminus” operations on the state manifold [23].

The correction step of IESKF is conducted by a Maximum A Posteriori (MAP) problem as in [20], where the prior distribution is obtained through state prediction, and the likelihood is obtained through the first-order approximation of point-to-plane measurement model [4].

$\mathcal{P}_k = \{p_j^{L_k} \mid j = 1, \dots, N_k\}$  is given at time  $k$ , the measurement model [4] is constructed based on the idea that a current point  $p_j^{L_k}$  acquired at time  $k$  should remain on a corresponding neighboring plane  $\pi_j$  in the map, as described below:

$$0 = \mathbf{h}_j(\mathbf{x}_k, p_j^{L_k} + \boldsymbol{\varepsilon}_j^{L_k}) = (\mathbf{u}_j^{L_0})^T (\mathbf{T}_{L_k}^{L_0} (p_j^{L_k} + \boldsymbol{\varepsilon}_j^{L_k}) - \mathbf{q}_j^{L_0}) \quad (6)$$

where  $\mathbf{u}_j^{L_0}$  is the unit normal vector of the nearest corresponding plane defined w.r.t  $\{L_0\}$ ;  $\mathbf{T}_{L_k}^{L_0}$  represent a LiDAR pose including  $(\mathbf{R}_{L_k}, \mathbf{p}_{L_k})$ , and the point  $\mathbf{q}_j^{L_0}$  is a LiDAR

point located on the plane within the map. By applying the first-order approximation to (6), we obtain

$$\begin{aligned} 0 &= \mathbf{h}_j(\mathbf{x}_k, p_j^{L_k} + \varepsilon_j^{L_k}) \\ &\simeq \mathbf{h}_j(\hat{\mathbf{x}}_k, p_j^{L_k} + 0) + \mathbf{H}_j \tilde{\mathbf{x}}_k + \mathbf{v}_j = \mathbf{z}_j + \mathbf{H}_j \tilde{\mathbf{x}}_k + \mathbf{v}_j \end{aligned} \quad (7)$$

where  $\mathbf{z}_j = \mathbf{h}_j(\hat{\mathbf{x}}_k, p_j^{L_k} + 0)$ ,  $\mathbf{H}_j = \left. \frac{\partial \mathbf{h}_j}{\partial \mathbf{x}_k} \right|_{\mathbf{x}_k = \hat{\mathbf{x}}_k}$ , and  $\mathbf{v}_j \in \mathcal{N}(\mathbf{0}, \mathbf{R}_j)$  is the disturbance which comes from the raw measurement noise  $\varepsilon_j^{L_k}$ .

Different from [20], however, we enhance the LO by *exploiting the planar constraint* which effectively reduces drift in the LO. Specifically, we further use the constraint that the roll and pitch of the rotation matrix  $\mathbf{R}_{L_k}$  and the z-component of the translation vector  $\mathbf{p}_{L_k}$  should be consistent because the motion of the robot is restricted to a 2D space. Thus, when we are given a normal vector  $\mathbf{n}_{L_k}$  of the LiDAR ground points  $\mathcal{G}_k$  at time  $k$ , the vector  $\mathbf{n}_{L_k}$  should be orthogonal to the x-y plane of the ground frame  $\{G\}$ .

$$\left[ \mathbf{R}_L^G \mathbf{R}_{L_k} (\mathbf{n}_{L_k} + \varepsilon_{\mathbf{n}_k}) \right]_{1,2} = 0 \quad (8)$$

where  $\varepsilon_{\mathbf{n}_k}$  is the observation noise to  $\mathbf{n}_{L_k}$ .  $[\cdot]_{1,2}$  denotes the notation that takes only the first and second elements in a  $(3 \times 1)$  vector is used. Further, the displacement of the z-component of  $\mathbf{p}_{L_k}$  should be zero respect to ground frame  $\{G\}$ , that is,

$$\mathbf{e}_3^T \mathbf{R}_L^G \mathbf{p}_{L_k} = 0. \quad (9)$$

By combining (8) and (9), we define a ground plane measurement model  $\mathbf{h}_\pi$  given by

$$0 = \mathbf{h}_\pi(\mathbf{x}_k, \mathbf{n}_{L_k} + \varepsilon_{\mathbf{n}_k}) = \begin{pmatrix} \left[ \mathbf{R}_L^G \mathbf{R}_{L_k} (\mathbf{n}_{L_k} + \varepsilon_{\mathbf{n}_k}) \right]_{1,2} \\ \mathbf{e}_3^T \mathbf{R}_L^G \mathbf{p}_{L_k} \end{pmatrix} \quad (10)$$

Using (10), by applying the first-order approximation, we derive the following equation,

$$\begin{aligned} 0 &= \mathbf{h}_\pi(\mathbf{x}_k, \mathbf{n}_{L_k} + \varepsilon_{\mathbf{n}_k}) \\ &\simeq \mathbf{h}_\pi(\hat{\mathbf{x}}_k, \mathbf{n}_{L_k} + 0) + \mathbf{H}_\pi \tilde{\mathbf{x}}_k + \mathbf{v}_\pi = \mathbf{z}_\pi + \mathbf{H}_\pi \tilde{\mathbf{x}}_k + \mathbf{v}_\pi \end{aligned} \quad (11)$$

where  $\mathbf{z}_\pi = \mathbf{h}_\pi(\hat{\mathbf{x}}_k, \mathbf{n}_{L_k} + 0)$ ,  $\mathbf{H}_\pi = \left. \frac{\partial \mathbf{h}_\pi}{\partial \mathbf{x}_k} \right|_{\mathbf{x}_k = \hat{\mathbf{x}}_k}$ , and  $\mathbf{v}_\pi \sim \mathcal{N}(\mathbf{0}, \mathbf{S}_k)$ .

By integrating the two likelihoods given by  $\mathbf{h}_j$  in (7) and our proposed  $\mathbf{h}_\pi$  in (10) apply to MAP estimate, we obtain  $\tilde{\mathbf{x}}_k$  by

$$\min_{\tilde{\mathbf{x}}_k^\tau} \left( \|\mathbf{x}_k \ominus \hat{\mathbf{x}}_k\|_{\mathbf{P}_k}^2 + \sum_{j=1}^m \|\mathbf{z}_j^\tau + \mathbf{H}_j \tilde{\mathbf{x}}_k^\tau\|_{\mathbf{R}_j}^2 + \|\mathbf{z}_\pi^\tau + \mathbf{H}_\pi \tilde{\mathbf{x}}_k^\tau\|_{\mathbf{S}_k}^2 \right) \quad (12)$$

where  $\tau$  means the number of iterate times.  $m$  is the number of LiDAR points. When  $\tilde{\mathbf{x}}_k$  decreases below a certain threshold, the state is considered to be optimal. Based on the optimal state  $\bar{\mathbf{x}}_k$  we return,

$$\mathbb{L}_k = \{\boldsymbol{\omega}_{L_k}, \mathbf{v}_{L_k}, \boldsymbol{\alpha}_{L_k}, \mathbf{a}_{L_k}\} \quad (13)$$

In (13),  $\boldsymbol{\omega}_{L_k}$  and  $\mathbf{v}_{L_k}$  are obtained from  $\bar{\mathbf{x}}_k$ , and the angular acceleration  $\boldsymbol{\alpha}_{L_k}$  and the linear acceleration  $\mathbf{a}_{L_k}$  of the LiDAR are computed by applying non-causal central difference [24] to  $\boldsymbol{\omega}_{L_k}$  and  $\mathbf{v}_{L_k}$ , respectively.

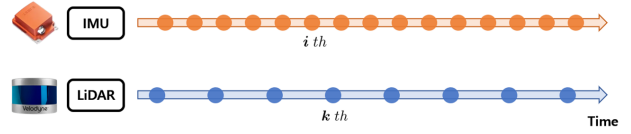


Fig. 3: Visualization of timestamp for each IMU measurement and LiDAR Odometry.

### C. IMU Processing and Synchronization with LiDAR Odometry

In general, the IMU measurement model is defined as follows.

$$\hat{\boldsymbol{\omega}}_i = \boldsymbol{\omega}_i + \mathbf{b}_g + \varepsilon_g, \quad \hat{\mathbf{a}}_i = \mathbf{a}_i + \mathbf{R}_{I_i}^w \mathbf{g}^w + \mathbf{b}_a + \varepsilon_a \quad (14)$$

The raw gyroscope and acceleration measurements at time  $i$  denote as  $\hat{\boldsymbol{\omega}}_i$  and  $\hat{\mathbf{a}}_i$ .  $\mathbf{b}_g$  is the gyroscope bias and  $\varepsilon_g$  is the gaussian white noise for the gyroscope measurement. Also,  $\mathbf{b}_a$  is the acceleration bias and  $\mathbf{g}^w$  is the gravity vector relative to world frame  $w$ , and  $\varepsilon_a$  is a Gaussian white noise for the acceleration measurement. Here, it should be noted that the IMU measurements are much faster than LO, we use two different time indices  $i$  and  $k$  for IMU and LO, respectively, as shown in Fig 3.

Similar to [20], we remove the noise  $\varepsilon_g$  and  $\varepsilon_a$  from the IMU measurements with a zero-phase filter [25] in 14. Also, we down-sample to get the IMU measurement at timestamp  $k$  from the LiDAR.

$$\bar{\boldsymbol{\omega}}_{I_k} = \boldsymbol{\omega}_{I_k} + \mathbf{b}_g, \quad \bar{\mathbf{a}}_{I_k} = \mathbf{a}_{I_k} + \mathbf{R}_{I_k}^w \cdot \mathbf{g}^w + \mathbf{b}_a \quad (15)$$

To achieve more precise synchronization between two sensors, we employ a coarse-to-fine approach to determine the time offset, denoted as  $t_L^I$ . As outlined in [20],  $t_L^I$  is the sum of the coarse estimate  $t_c$  and the fine estimate  $t_f$ , thereby defined as  $t_L^I = t_c + t_f$ . Similar to [20], we determine  $t_c$  by using the cross-correlation method given by

$$t_c^* = \arg \max_{t_c} \sum_{k=1}^n \|\bar{\boldsymbol{\omega}}_{I_k+t_c}\| \cdot \|\boldsymbol{\omega}_{L_k}\| \quad (16)$$

In the following section, we derive the remaining component,  $t_f$ , as the outcome of the optimization process. Further, by applying the IMU measurements  $\boldsymbol{\omega}_{I_k}$  and  $\mathbf{a}_{I_k}$  to the Madgwick filter [21], we estimate the rotation matrix  $\mathbf{R}_I^G$  from the ground frame  $\{G\}$  to the IMU frame  $\{I\}$ . Finally, as a result from the IMU processing and synchronization procedure, we return

$$\mathbb{I}_k = \{\bar{\boldsymbol{\omega}}_{I_k}, \bar{\boldsymbol{\alpha}}_{I_k}, \bar{\mathbf{a}}_{I_k}, \mathbf{R}_I^G\} \quad (17)$$

## V. EXTRINSIC CALIBRATION VIA SINGLE OPTIMIZATION (SO)

Using the two sets of measurements  $\mathbb{L}_k$  in (13) and  $\mathbb{I}_k$  in (17) obtained from Section IV, we formulate the IMU-LiDAR extrinsic calibration as an optimization problem. The calibration parameter  $\mathbf{x}_{cal}$  used in the calibration is given by,

$$\mathbf{x}_{cal} = [\mathbf{R}_L^I, \mathbf{p}_L^I, t_f, \mathbf{b}_g, \mathbf{b}_a] \quad (18)$$



### A. Unified Temporal-Spatial Constraints

We jointly utilize the two constraints proposed in [20]. The first constraint uses the angular velocity measurements  $\bar{\omega}_{I_k}$  and  $\omega_{L_k}$  from IMU measurements and LO, respectively.

$$\bar{\omega}_{I_{k'}} + t_f \cdot \bar{\alpha}_{I_{k'}} = (\mathbf{R}_L^I)^T \omega_{L_k} + \mathbf{b}_g \quad (19)$$

by compensating the time offset  $k' = k + t_c^*$  between two sensors, where  $t_c^*$  is given in 16 and assuming the IMU angular acceleration  $\bar{\alpha}_{I_{k'}}$  is constant over a small period of time  $t_f$ . This is described as follows, according to (19)

$$\mathbf{r}_w(\mathbf{R}_L^I, \mathbf{b}_g, \mathbf{t}_f) = (\mathbf{R}_L^I)^T \omega_{L_k} + \mathbf{b}_g - \bar{\omega}_{I_{k'}} - t_f \cdot \bar{\alpha}_{I_{k'}} \quad (20)$$

The second constraint uses the acceleration measurements  $\bar{\mathbf{a}}_{I_k}$  and  $\mathbf{a}_{L_k}$  from IMU and LO, respectively. As in [26], the accelerations  $\mathbf{a}_{I_k}$  and  $\mathbf{a}_{L_k}$  of the two sensors are related to each other by

$$\mathbf{R}_L^I \bar{\mathbf{a}}_I = \mathbf{a}_L + \{([\omega_L]_{\times}^2 + [\alpha_L]_{\times}) \cdot \mathbf{p}_L^I\} \quad (21)$$

where  $\alpha_L$  is obtained from  $\mathbb{L}_k$ . the second constraint  $\mathbf{r}_a$  is represented as follows.

$$\mathbf{r}_a(\mathbf{R}_L^I, \mathbf{p}_L^I, \mathbf{b}_a) = \mathbf{R}_L^I (\bar{\mathbf{a}}_{I_{k'}} - \mathbf{b}_a) - \mathbf{a}_{L_k} - \{([\omega_{L_k}]_{\times}^2 + [\alpha_{L_k}]_{\times}) \cdot \mathbf{p}_L^I\} \quad (22)$$

### B. Ground Plane Motion Constraints

In this subsection, we describe a novel constraint named Ground Plane Motion (GPM). Our proposed constraint is slightly similar to the constraint proposed in [13], where the plane motion information was leveraged to improve the performance of VINS. However, the constraint in [13] was formulated for the estimation of sensor motion, while our constraint is specifically designed for extrinsic calibration between IMU and LiDAR. Specifically, our GPM is parameterized in terms of  $\mathbf{R}_L^I$  and  $\mathbf{p}_L^I$ . In the formulation of the GPM, we directly measure the height of the IMU from the ground  $\hat{d}_I \in \mathbb{R}$  and use it as prior knowledge. Further, we exploit the fact that the z-component of  $\mathbf{p}_L^I$  could not be observed because it is in the direction perpendicular to the planar motion. Using the geometric relationship of the rotation parameters between the ground and each sensor shown in Fig 4, we obtain

$$[\mathbf{R}_I^G \mathbf{R}_L^I \mathbf{R}_G^L \mathbf{e}_3]_{1,2} = 0 \quad (23)$$

$$\mathbf{e}_3^T (\mathbf{R}_L^I \mathbf{R}_G^L \mathbf{d}_I - \mathbf{R}_G^L \mathbf{d}_L) = \mathbf{e}_3^T \mathbf{p}_L^I \quad (24)$$

where  $\mathbf{d}_L = d_L \mathbf{e}_3$ , and  $d_L$  is the height of the LiDAR from the ground and it is obtained from (1).  $\mathbf{d}_I = \hat{d}_I \mathbf{e}_3$ , and  $\hat{d}_I$  denotes the height of the IMU from the ground ( $\mathbf{R}_L^G$ )<sup>T</sup> =  $\mathbf{R}_G^L$  and ( $\mathbf{R}_I^G$ )<sup>T</sup> =  $\mathbf{R}_G^I$ , and they are obtained from (1) and (17), respectively. The proposed Ground Plane Motion (GPM) constraint  $\mathbf{r}_g$  is represented as

$$\mathbf{r}_g(\mathbf{R}_L^I, \mathbf{p}_L^I) = \begin{pmatrix} [\mathbf{R}_I^G \mathbf{R}_L^I \mathbf{R}_G^L \mathbf{e}_3]_{1,2} \\ \mathbf{e}_3^T (\mathbf{R}_L^I \mathbf{R}_G^L \mathbf{d}_I - \mathbf{R}_G^L \mathbf{d}_L - \mathbf{p}_L^I) \end{pmatrix} \quad (25)$$

Unlike [7], which performs the calibration while ignoring unobservable direction, our *Gril-Calib* conducts extrinsic calibration including unobservable direction even under the planar motion by utilizing Ground Plane Motion (GPM) constraints.

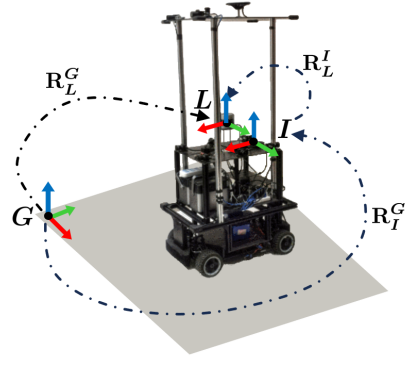


Fig. 4: Illustration of the geometric rotation relationship between ground and each sensor. This robot platform is used in the M2DGR dataset.

### C. Single Optimization (SO) Process

The method proposed in [20] uses two distinct constraints,  $\mathbf{r}_w$  and  $\mathbf{r}_a$ , separately over the two-stage optimization process. First,  $\mathbf{R}_L^I$  is obtained by minimizing the residual  $\mathbf{r}_w$ , and then  $\mathbf{p}_L^I$  is determined by minimizing the residual  $\mathbf{r}_a$  in [20]. However, this approach overlooks the interaction and correlation between these constraints. Specifically, the residual  $\mathbf{r}_a$  depends on not only  $\mathbf{p}_L^I$  but also  $\mathbf{R}_L^I$  simultaneously. In our *Gril-Calib*, we address this ineffectiveness by reformulating the calibration as a Single Optimization (SO). Our optimization problem could be depicted as follows,

$$\mathbf{x}_{cal}^* = \arg \min_{\mathbf{x}} \sum \{ \rho_w \|\mathbf{r}_w(\mathbf{R}_L^I, \mathbf{b}_g, \mathbf{t}_f)\|_{\Sigma_{r_w}}^2 + \rho_a \|\mathbf{r}_a(\mathbf{R}_L^I, \mathbf{p}_L^I, \mathbf{b}_a)\|_{\Sigma_{r_a}}^2 + \rho_g \|\mathbf{r}_g(\mathbf{R}_L^I, \mathbf{p}_L^I)\|_{\Sigma_{r_g}}^2 \} \quad (26)$$

and minimize the two residuals  $\mathbf{r}_w$  and  $\mathbf{r}_a$  along with our proposed residual  $\mathbf{r}_g$  simultaneously, where  $\Sigma_{r_w}, \Sigma_{r_a}, \Sigma_{r_g}$  denotes the Mahalanobis distance for each covariance matrix.  $\rho_x$ , where  $x = w, a, g$  refers to the scaled Cauchy kernel function assigned to each residual.

## VI. EXPERIMENTS

### A. Experiments Setup

Our implementation is based on C++, using ROS (Robot Operating System) on Ubuntu 18.04. We perform our experiments using a 4-core Intel® Core™ i5-6600 CPU and Titan XP GPU. We use Ceres-solver<sup>2</sup> to compute the non-linear optimization. We evaluated the algorithms using three public datasets: M2DGR [14], Hilti [15], and S3E [16], which cover both indoor and outdoor environments. Following the evaluation scheme used in [20], we only evaluate spatial extrinsic calibration parameters in terms of RMSE (Root Mean Squared Error), skipping the evaluation on IMU LiDAR time offset  $t_L^I$ . To show the effectiveness of our *Gril-Calib*, we compare our method with other recent IMU-LiDAR calibration methods which are named ILC [18], FAST-LIO2 [4], OA-LICalib [11], LI-Init [20]. All algorithms are reproduced in the same environment.

<sup>2</sup><http://ceres-solver.org/>

TABLE I: RMSE result compared to existing methods on M2DGR dataset

M2DGR [14]	Gate 01 [0, 140]		Rotation 02 [0, 120]		Hall 04 [0, 160]		Lift 04 [0, 80]		Street 08 [20, 130]	
	Rotation (°)	Translation (m)	Rotation (°)	Translation (m)	Rotation (°)	Translation (m)	Rotation (°)	Translation (m)	Rotation (°)	Translation (m)
ICL [18]	29.549	1.210	11.581	0.839	48.628	7.517	9.998	0.390	7.205	0.847
FAST-LIO2 [4]	3.388	0.392	3.686	0.394	3.325	0.387	3.667	0.401	3.335	0.385
OA-LiCalib [11]	0.642	0.237	0.922	0.208	0.851	1.742	0.902	<b>0.021</b>	0.770	0.241
LI-Init [20]	1.120	0.383	1.305	0.311	2.108	0.236	0.904	0.263	0.784	0.223
GRIL-Calib (Proposed)	<b>0.376</b>	<b>0.045</b>	<b>0.818</b>	<b>0.033</b>	<b>0.472</b>	<b>0.027</b>	<b>0.154</b>	0.066	<b>0.328</b>	<b>0.043</b>

The best-performing algorithms are shown in **bold**.

### B. Extrinsic Calibration Performance on the M2DGR

The calibration result on the M2DGR dataset is summarized in Table I. M2DGR uses Velodyne VLP-32C as the LiDAR and Handsfree A9 as the IMU. For a consistent comparison, the initial rotation and translation parameters are set to be the same for all algorithms. The initial rotation parameters are set to  $\mathbf{R}_L^I = (-5.0, -5.0, 5.0)$  with the unit in degrees. The initial translation parameters deviated by 0.402 meters from the ground truth based on RMSE, represented as  $\mathbf{p}_L^I = (0.6, 0.45, 0.6)$ . We initialized all remaining state vectors  $\mathbf{t}_f, \mathbf{b}_g, \mathbf{b}_a$  to zeros. Data was collected from both indoor (*Hall 04* and *Lift 04*) and outdoor (*Gate 01*, *Rotation 02*, and *Street 08*) environments, with partial visualizations provided in Fig 5. The calibration result on the M2DGR is summarized in Table I. The table shows that our Gril-Calib significantly outperforms the other competing methods, specifically reducing RMSE by 75% for rotations and 79% for translations compared to the baseline [20].

The extrinsic parameters of each calibration method are visualized in Fig. 6. Fig. 6a and Fig. 6b are the results of the rotation and translation matrices, respectively. In both figures, the dotted lines denote the ground truth of the extrinsic parameters. Thus, the closer to the dotted line, the better the calibration method is. ICL [18] is excluded from the figure because its error is significantly larger than that of the other methods.

### C. Extrinsic Calibration Performance on the Others

S3E and HILTI data are used as additional datasets, and their results are summarized in Table II and Table III, respectively. Both of the datasets are captured indoors. The S3E dataset uses a Velodyne VLP-16 and Xsens MTi-30 IMU, while the HILTI dataset uses an Ouster OS0-64 LiDAR and AlphaSense IMU. As shown in Tables II and

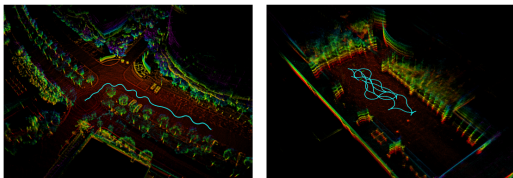
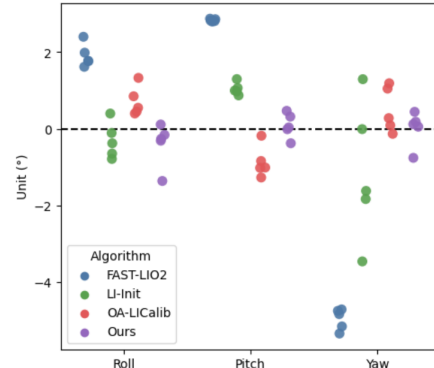
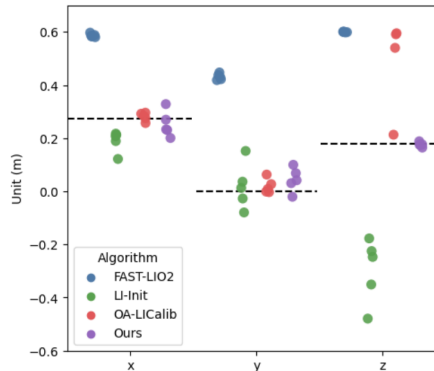


Fig. 5: Trajectory visualization for *Street 08* acquired outdoors (Left), and *Hall 04* acquired indoors (Right). We evaluated the algorithm with data collected from a variety of environments.



(a) IMU-LiDAR extrinsic rotation parameters results



(b) IMU-LiDAR extrinsic translation parameter results

Fig. 6: Visualization for each of the extrinsic parameters. The dotted line represents the ground truth. Closer to the dotted line represents the best estimation.

III, our algorithm outperforms other competing methods as in M2DGR, and it shows the reliable accuracy of our *Gril-Calib* across various robot platforms. We also observe that OA-LiCalib fails in calibration due to a memory computation issue in the *Baseline 3* sequence in Table III. The reason might be that OA-LiCalib uses surfel maps for calibration and the computational cost rapidly increases with the number of surfels. In contrast, our algorithm works smoothly without any memory issues. The two tables along with Table I show the effectiveness and versatility of our approach in various real-world scenarios.

### D. Robustness to the Initial Guess

The extrinsic calibration usually requires initial parameter values, and it significantly affects the performance [27]. We

TABLE II: RMSE result compared to existing methods on S3E dataset

S3E [16]	<i>Lab 01</i> ( $\beta$ ) [65, 210]		<i>Lab 02</i> ( $\beta$ ) [220, 340]	
	Rotation ( $^\circ$ )	Translation (m)	Rotation ( $^\circ$ )	Translation (m)
ICL [18]	6.430	0.288	9.817	0.813
FAST-LIO2 [4]	3.489	0.303	3.351	0.300
OA-LICalib [11]	0.339	0.194	18.512	0.321
LI-Init [20]	1.238	0.116	1.657	0.066
GRIL-Calib (Proposed)	<b>0.935</b>	<b>0.036</b>	<b>0.847</b>	<b>0.027</b>

TABLE III: RMSE result compared to existing methods on HILTI dataset

HILTI [15]	<i>Basement 3</i> [85, 315]		<i>Basement 4</i> [75, 225]	
	Rotation ( $^\circ$ )	Translation (m)	Rotation ( $^\circ$ )	Translation (m)
ICL [18]	13.308	4.555	44.294	4.052
FAST-LIO2 [4]	1.964	0.196	1.892	0.188
OA-LICalib [11]	×	×	2.368	0.185
LI-Init [20]	<b>0.374</b>	0.092	2.584	0.194
GRIL-Calib (Proposed)	0.716	<b>0.018</b>	<b>0.589</b>	<b>0.047</b>

× means that the algorithm failed.

conduct some experiments while varying initial guesses to see how robust the competing calibration methods are to the initial guesses. We use *Gate 01* sequence in M2DGR. The results are shown in Fig 8. Fig 8a shows the change of the calibration error while fixing the initial  $\mathbf{p}_L^I$  but changing initial  $\mathbf{R}_L^I$ . Fig 8b is the result when  $\mathbf{R}_L^I$  is fixed but  $\mathbf{p}_L^I$  is varied. Interestingly, OA-LICalib showed relatively good performance in the previous three datasets, but as the initial guess increases, its accuracy rapidly degrades. Instead, LI-Init demonstrates robust performance against the initial guess, but it is less accurate than our Gril-Calib due to the limited planar motion.

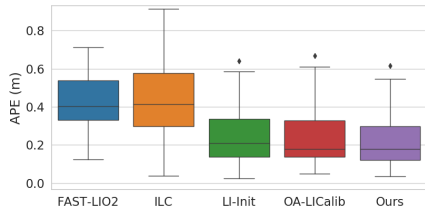
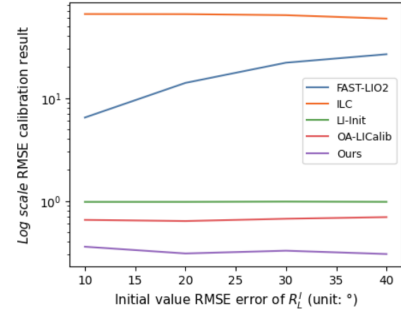


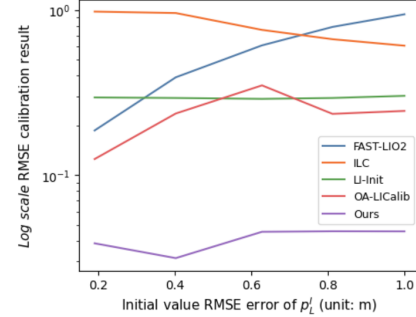
Fig. 7: Evaluation of LiDAR-inertial odometry using different calibration algorithms.

TABLE IV: Ablation study for proposed method

	GPM	SO	LO w/ GP	RMSE	
				Rotation ( $^\circ$ )	Translation (m)
LI-Init [20] (Baseline)				1.710	0.300
GRIL-Calib (Proposed)	✓	✓		1.421	0.088
	✓	✓		0.685	0.054
	✓	✓	✓	<b>0.430</b>	<b>0.041</b>



(a) RMSE result of IMU-LiDAR extrinsic rotation parameters  $\mathbf{R}_L^I$



(b) RMSE result of IMU-LiDAR extrinsic translation parameters  $\mathbf{p}_L^I$

Fig. 8: Calibration performance with changes initial guess.

### E. Application to IMU-LiDAR Fusion System

We compare the competing extrinsic calibration methods by applying the respective results to IMU-LiDAR fusion system and evaluating the corresponding odometry accuracy. In the experiment, we utilize Faster-LIO [6] as the IMU-LiDAR fusion system. The results in Table I used extrinsic parameters of each method. The experiment uses the *hall 02* sequence since the sequence was not used in Subsection VI-B. The Absolute Pose Error (APE) is depicted from different calibration methods in Fig 7. We observe that the odometry obtained by our *Gril-Calib* outperforms those of other methods. In particular, our *Gril-Calib* achieves 8.6% improvement from LI-Init and 9.6% improvement from OA-LICalib. This experiment shows the importance of accurate calibration when applied to IMU-LiDAR fusion systems.

### F. Ablation Study

We ablate three key modules comparing the result with that of our baseline [20]. The results are summarized in Table IV.

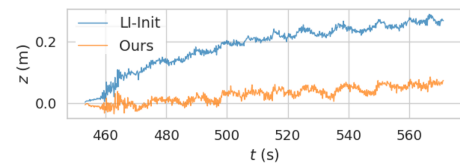


Fig. 9: Comparative visualization of the z-component of a trajectory using *Rotation 02* sequence in M2DGR.

On the first row of the table, ‘GPM’, ‘SO’, and ‘LO w/ GP’ denote the three contributions made in our paper. That is, they imply ‘calibration using GPM constraints’, ‘calibration via single optimization’, and ‘LO with proposed ground plane residual’, respectively. Notably, SO observed a 34% decrease in RMSE for translation calibration. This reduction highlights that  $\mathbf{R}_L^I$  and  $\mathbf{p}_L^I$  are highly correlated and the separate optimization which ignores the correlation would lead to degraded accuracy. Our LO method with the proposed ground plane residual, effectively minimizes z-axis drift in the LO, as shown in Fig 9. This drift reduction leads to more stable and accurate measurements, thereby enhancing the overall precision of our calibration approach.

## VII. CONCLUSIONS

In this paper, we present *GRIL-Calib*: a novel targetless IMU-LiDAR extrinsic calibration framework that mainly focuses on the ground robot. Our framework aimed to address the challenge of obtaining accurate 6-DoF extrinsic parameters including unobservable direction when the robot’s motion is limited to a planar motion. To achieve this, we proposed the Ground Plane Motion (GPM) constraint to utilize ground observation, which is easily accessible for the ground robots. We also reformulate the calibration as a Single Optimization (SO) problem to take advantage of the correlation of the residuals. Additionally, we proposed ground plane residual to reduce the z-drift of the LiDAR odometry, thereby improving the accuracy of the calibration. Finally, we demonstrated the effectiveness and reliability of our *GRIL-Calib* by applying it to three public datasets and varying some initial calibration parameters. We acknowledge that our algorithm’s performance might be affected by uneven ground. Future works should focus on calibration for such terrains.

## REFERENCES

- [1] I. Vizzo, T. Guadagnino, B. Mersch, L. Wiesmann, J. Behley, and C. Stachniss, “Kiss-icp: In defense of point-to-point icp—simple, accurate, and robust registration if done the right way,” *IEEE Robotics and Automation Letters*, vol. 8, no. 2, pp. 1029–1036, 2023.
- [2] J. Wang, M. Xu, G. Zhao, and Z. Chen, “3d lidar localization based on novel nonlinear optimization method for autonomous ground robot,” *IEEE Transactions on Industrial Electronics*, 2023.
- [3] J. Zhang and S. Singh, “Loam: Lidar odometry and mapping in real-time.” in *Robotics: Science and systems*, vol. 2, no. 9. Berkeley, CA, 2014, pp. 1–9.
- [4] W. Xu, Y. Cai, D. He, J. Lin, and F. Zhang, “Fast-lio2: Fast direct lidar-inertial odometry,” *IEEE Transactions on Robotics*, vol. 38, no. 4, pp. 2053–2073, 2022.
- [5] T. Shan, B. Englot, D. Meyers, W. Wang, C. Ratti, and D. Rus, “Lio-sam: Tightly-coupled lidar inertial odometry via smoothing and mapping,” in *2020 IEEE/RSJ International conference on intelligent robots and systems (IROS)*. IEEE, 2020, pp. 5135–5142.
- [6] C. Bai, T. Xiao, Y. Chen, H. Wang, F. Zhang, and X. Gao, “Faster-lio: Lightweight tightly coupled lidar-inertial odometry using parallel sparse incremental voxels,” *IEEE Robotics and Automation Letters*, vol. 7, no. 2, pp. 4861–4868, 2022.
- [7] S. Li, X. Li, Y. Zhou, and C. Xia, “Targetless extrinsic calibration of lidar–imu system using raw gnss observations for vehicle applications,” *IEEE Transactions on Instrumentation and Measurement*, vol. 72, pp. 1–11, 2023.
- [8] W. Liu and Y. Li, “Error modeling and extrinsic–intrinsic calibration for lidar–imu system based on cone–cylinder features,” *Robotics and Autonomous Systems*, vol. 114, pp. 124–133, 2019.
- [9] Y. Yang, P. Geneva, K. Eickenhoff, and G. Huang, “Degenerate motion analysis for aided ins with online spatial and temporal sensor calibration,” *IEEE Robotics and Automation Letters*, vol. 4, no. 2, pp. 2070–2077, 2019.
- [10] Y. Yang, P. Geneva, X. Zuo, and G. Huang, “Online self-calibration for visual-inertial navigation: Models, analysis, and degeneracy,” *IEEE Transactions on Robotics*, 2023.
- [11] J. Lv, X. Zuo, K. Hu, J. Xu, G. Huang, and Y. Liu, “Observability-aware intrinsic and extrinsic calibration of lidar-imu systems,” *IEEE Transactions on Robotics*, vol. 38, no. 6, pp. 3734–3753, 2022.
- [12] X. Wei, J. Lv, J. Sun, E. Dong, and S. Pu, “Gclo: Ground constrained lidar odometry with low-drifts for gps-denied indoor environments,” in *2022 International Conference on Robotics and Automation (ICRA)*. IEEE, 2022, pp. 2229–2235.
- [13] H. Li and J. Stueckler, “Visual-inertial odometry with online calibration of velocity-control based kinematic motion models,” *IEEE Robotics and Automation Letters*, vol. 7, no. 3, pp. 6415–6422, 2022.
- [14] J. Yin, A. Li, T. Li, W. Yu, and D. Zou, “M2dgr: A multi-sensor and multi-scenario slam dataset for ground robots,” *IEEE Robotics and Automation Letters*, vol. 7, no. 2, pp. 2266–2273, 2021.
- [15] M. Helmberger, K. Morin, B. Berner, N. Kumar, G. Cioffi, and D. Scaramuzza, “The hilti slam challenge dataset,” *IEEE Robotics and Automation Letters*, vol. 7, no. 3, pp. 7518–7525, 2022.
- [16] D. Feng, Y. Qi, S. Zhong, Z. Chen, Y. Jiao, Q. Chen, T. Jiang, and H. Chen, “S3e: A large-scale multimodal dataset for collaborative slam,” *arXiv preprint arXiv:2210.13723*, 2022.
- [17] C. Le Gentil, T. Vidal-Calleja, and S. Huang, “3d lidar-imu calibration based on upsampled preintegrated measurements for motion distortion correction,” in *2018 IEEE International Conference on Robotics and Automation (ICRA)*, 2018, pp. 2149–2155.
- [18] S. Mishra, G. Pandey, and S. Saripalli, “Target-free extrinsic calibration of a 3d-lidar and an imu,” in *2021 IEEE International Conference on Multisensor Fusion and Integration for Intelligent Systems (MFI)*. IEEE, 2021, pp. 1–7.
- [19] J. Lv, J. Xu, K. Hu, Y. Liu, and X. Zuo, “Targetless calibration of lidar-imu system based on continuous-time batch estimation,” in *2020 IEEE/RSJ International Conference on Intelligent Robots and Systems (IROS)*. IEEE, 2020, pp. 9968–9975.
- [20] F. Zhu, Y. Ren, and F. Zhang, “Robust real-time lidar-inertial initialization,” in *2022 IEEE/RSJ International Conference on Intelligent Robots and Systems (IROS)*. IEEE, 2022, pp. 3948–3955.
- [21] S. Madgwick *et al.*, “An efficient orientation filter for inertial and inertial/magnetic sensor arrays,” *Report x-io and University of Bristol (UK)*, vol. 25, pp. 113–118, 2010.
- [22] S. Lee, H. Lim, and H. Myung, “Patchwork++: Fast and robust ground segmentation solving partial under-segmentation using 3d point cloud,” in *2022 IEEE/RSJ International Conference on Intelligent Robots and Systems (IROS)*. IEEE, 2022, pp. 13 276–13 283.
- [23] C. Hertzberg, R. Wagner, U. Frese, and L. Schröder, “Integrating generic sensor fusion algorithms with sound state representations through encapsulation of manifolds,” *Information Fusion*, vol. 14, no. 1, pp. 57–77, 2013.
- [24] D. Baleanu, O. Defterli, and O. P. Agrawal, “A central difference numerical scheme for fractional optimal control problems,” *Journal of Vibration and Control*, vol. 15, no. 4, pp. 583–597, 2009.
- [25] F. Gustafsson, “Determining the initial states in forward-backward filtering,” *IEEE Transactions on signal processing*, vol. 44, no. 4, pp. 988–992, 1996.
- [26] W. Xu, D. He, Y. Cai, and F. Zhang, “Robots’ state estimation and observability analysis based on statistical motion models,” *IEEE Transactions on Control Systems Technology*, vol. 30, no. 5, pp. 2030–2045, 2022.
- [27] S. Xu, J. S. Willners, Z. Hong, K. Zhang, Y. R. Petillot, and S. Wang, “Observability-aware active extrinsic calibration of multiple sensors,” in *2023 IEEE International Conference on Robotics and Automation (ICRA)*. IEEE, 2023, pp. 2091–2097.